Physics of Fluids

RESEARCH ARTICLE | AUGUST 18 2022

Orientation dynamics of anisotropic and polydisperse colloidal suspensions

Narges Mohammad Mehdipour; Naveen Reddy; Roman J. Shor; ... et. al

Physics of Fluids 34, 083317 (2022)
https://doi.org/10.1063/5.0101702

AIP Publishing

Physics of Fluids ARTICLE scitation.org/journal/phf

Orientation dynamics of anisotropic and polydisperse colloidal suspensions

Cite as: Phys. Fluids **34**, 083317 (2022); doi: 10.1063/5.0101702
Submitted: 2 June 2022 · Accepted: 23 July 2022 ·
Published Online: 18 August 2022

Narges Mohammad Mehdipour,[1] Naveen Reddy,[2,3] Roman J. Shor,[1] and Giovanniantonio Natale[1,a)]

AFFILIATIONS

[1] Department of Chemical and Petroleum Engineering, University of Calgary, 2500 University Drive NW, Calgary, Alberta T2N 1N4, Canada
[2] Institute for Materials Research (IMO-IMOMEC), Hasselt University, Diepenbeek, Belgium
[3] IMEC vzw, Division IMOMEC, Diepenbeek, Belgium

[a)] Author to whom correspondence should be addressed: gnatale@ucalgary.ca

ABSTRACT

Small-angle light scattering (SALS) is employed to determine *in situ* microstructural changes of polydisperse colloidal suspensions under capillary flow. Titanium dioxide (rod-like) bundles and kaolinite nanoclay (platelet) flake-like stacks of particles are suspended in a Newtonian fluid to explore the effects of shape anisotropy. Subjecting the systems to a startup test in a flow cell in Stokes's regime, the evolution of the anisotropy factor (AF), and the average orientation angle (χ) of particles vs strain is probed at different averaged Péclet ($\overline{\mathrm{Pe}}$) numbers. Dilute and semi-dilute concentration regimes are explored in a capillary flow. Moving in the vorticity direction, we show significant changes in χ due to the gradient in shear rate in the capillary flow, while no cross-sectional flow migration was exhibited. In these polydisperse colloidal suspensions, two characteristic stages are observed: initial particle alignment and subsequent orientational demixing. Probing the velocity–vorticity (xy) plane, an initial particle alignment in the flow direction at high $\overline{\mathrm{Pe}}$ (> 1) occurs, is demonstrated by an elliptical SALS pattern, and then, an increase in AF is observed due to particles' phase mixing. This behavior is then followed by a breakdown in structure and loss of particle alignment due to orientational demixing. The evolution of the average orientation angle of particles in the xy plane can be clearly observed through these two stages by the help of high-resolution SALS contours. These experimental findings provide novel insights into the flow–microstructure relationship of polydisperse colloidal suspensions for the optimization of many industrial processing schemes.

INTRODUCTION

Subjecting a colloidal suspension to flow can largely affect its microstructure. Industrial applications such as transportation of oil sands,[1] flow fractionation,[2] paint production,[3,4] cosmetics,[5] and engineered polymer nanocomposites in biomedical application[6–9] are examples where the suspended particle's properties and microstructures have a strong influence on the final process or material. These systems intrinsically contain a dispersed phase with length scales ranging from individual particles to aggregates.[10–12] Thus, a clear understanding of transient and steady-state behavior of polydisperse particle suspensions under flow is of essential importance to optimize such processes.[13] It is also noteworthy that real particles in nature are rarely perfect spheres. Non-spherical particles may be dragged along and rotated by flow, similar to spheres, but feel hydrodynamic stresses which depend on the orientation of particles relative to the flow direction.[14] Thus, stresses change during particle rotation and result in a time-dependent motion which depends on the shape of the particles. The shape anisotropy of a particle is characterized by its aspect ratio (r) which is defined as the ratio between the dimension along the symmetry axis (e.g., length of a rod or diameter of a platelet) and the one perpendicular to it.[15,16]

The equation of motion for an inertia-less ellipsoid in a linear flow field was first derived by Jeffery.[17] Jeffery's solution predicts that a high (but finite) aspect ratio particle with no inertia performs orbits in shear flow and spends most of its time in the direction of flow. Stover and Cohen[18] monitored the motion of non-Brownian rod-like particles freely suspended in Newtonian fluid at low Re numbers and between two parallel plates in a transparent flow cell. The time-dependent orientation of an elliptical particle far and near to the wall was found in quantitative agreement with Jeffery's theory in simple shear flow. Particles far from the wall could align with the flow direction, while particles with less than a particle half-length from the wall could not show the same behavior because of the excluded volume interactions and the steric interactions between particle and wall.[19] Goldsmith and Mason[20] explored the motion of non-Brownian and isolated particles with two shapes (fibers and platelets) representing a typical deviation from sphericity. The fiber's rotation slows down when its symmetry axis gets close to the flow direction due to the minimum torque on the particle. While for a disk with a comparable aspect ratio, the minimum torque is felt by the particle when its symmetry axis (thickness direction) is perpendicular to the flow direction.

In a homogenous dispersion of anisotropic particles, a multitude of particle orientations is present. The resulting state of such a system can be described by a probability distribution function (PDF).[21] Although for dilute non-Brownian particle suspensions the evolution of the system depends on the initial orientation distribution, colloidal systems lose this dependency due to their Brownian character.[22–24] The ratio of the randomization due to Brownian motion and the orientational distortion due to the flow is expressed by the rotational Péclet number, $\mathrm{Pe} = {}^{\dot{\gamma}}/_{\mathrm{D_r}}$, where $\dot{\gamma}$ is the shear rate magnitude of the flow field and $\mathrm{D_r}$ is the rotational diffusion of the particle. In contrast to spherical particles, orientation dynamics manifest in complex rheological responses such as shear thinning behavior and normal stresses even in the dilute regime of concentration.[1,14,15,25] Hence, the rheological properties of a suspension of anisotropic particles are strongly affected by the evolution of particles' PDF.[26] This PDF in real systems depends on hydrodynamic interactions, particle–particle interactions, inertia, and polydispersity in the shape or the size of the particles.[15,27–29] To understand only the effect of particle polydispersity, other contributions can be neglected by working in a non-interacting dilute concentration of axisymmetric density-matched particles.[30,31]

In polydisperse systems subjected to a spatially varying velocity, it is necessary to define an averaged Pe number ($\overline{\mathrm{Pe}}$), which is obtained by averaging the individual particles $\mathrm{D_r}$ or $\dot{\gamma}$ due to their size, shape, or local shear rate magnitude. The effect of particles' size polydispersity has been studied theoretically and experimentally only in nearly monodisperse systems using optical methods. For a system that contains monodisperse non-interacting and neutrally buoyant rigid ellipsoids dispersed in a Newtonian fluid, Okagawa *et al.*[32] derived an orientation distribution function ($\mathrm{p_t}$) which depends on time, orientational configuration, and the hydrodynamic aspect ratio of particles ($\mathrm{r_{ha}}$). By averaging $\mathrm{p_t}$, optical characteristics of dispersion can be derived such as linear dichroism and average orientation angle of particles. For monodisperse particles with an identical value of $\mathrm{r_{ha}}$, this equation results in an average orientation angle which oscillates indefinitely in time under steady shear flow. While for polydisperse systems, the orientation angle shows damped oscillation due to the variations in shape and size or $\mathrm{r_{ha}}$. The variation in particles' aspect ratio results in different angular velocities of the particles, and by increasing polydispersity, the correlation of particles' motion is quickly lost.[32,33] Johnson and Fuller[34] experimentally studied the average orientation angle of nearly monodisperse hematite rod-like particles ($\mathrm{r_a} \approx 2.5-6$) dispersed in a Newtonian medium and in a Couette flow device. By using dichroism and birefringence, they demonstrated that simple shear flow produces an average orientation angle as a function of the rotational Pe, in which the size, shape, and polydispersity of particles play an important role. These slightly polydisperse particles with moderate aspect ratios showed a characteristic oscillation in the average orientation angle in the vorticity plane resembling Jeffery orbits which damps to a steady-state value. This damping behavior was attributed to Brownian motion and polydispersity of the system. They also demonstrated that a polydisperse suspension containing a significant number of smaller particles with low $\overline{\mathrm{Pe}}$ spreads the orientation PDF of the system. Vermant *et al.*[35] related the polydispersity of the system to the average hydrodynamic aspect ratio of $\overline{\mathrm{r_{ha}}}$ by defining a Gaussian distribution function $\mathrm{g_{r_{ha}}}$. Based on these damping dynamics, Reddy *et al.*[36] developed a reliable method for calculating the particle aspect ratio and size polydispersity. To achieve this, they employed Brenner's model that relates the hydrodynamic dimension to the diffusion coefficients of the particles; originally, it was derived for infinitely thin rods[36,37] and then modified for small aspect ratio rods taking into account the end effect of the particles.[38] By comparing two shapes of gold particles, nanorod and nanodecahedral, and the theoretical predictions, they showed that light scattering is the most reliable method for calculating the particle aspect ratio and size polydispersity. While dynamic light scattering (DLS) was only useful for rods, dichroism could correctly find the particle hydrodynamic aspect ratio and shows the damping behavior of average orientation angle by increasing the polydispersity of particle size.

There are also other possible reasons for the damping of the oscillations of the average orientation angle such as interactions between particles.[35,39] To study the effect of such interactions, carbon nanotube systems were used which can be considered thin and long rigid rods.[40] The anisotropy of polydisperse suspensions of sheared carbon nanotubes in a semi-dilute regime was studied by Fry *et al.*[41] in the velocity–vorticity plane of a Couette shear cell. They used small-angle neutron scattering (SANS) to investigate the dilute regime of single-wall nanotubes (SWNT) and small-angle light scattering (SALS) to study the semi-dilute suspensions of multiwall nanotubes (MWNT) in Newtonian and non-Newtonian fluids. Their results show that the order parameter of the semi-dilute regime of MWNT is larger than that of SWNT in the dilute regime which reflects the larger aspect ratio of MWNTs. These semi-dilute systems show a flow-fractionation in the non-Newtonian medium at a high $\overline{\mathrm{Pe}}$ ($\approx 10^6$) number in which the shorter particles migrate toward shearing surfaces and longer particles migrate into the bulk while aligned in the flow direction. Natale *et al.*[42] also investigated the orientation of MWNT dispersion in a Newtonian matrix ranging from dilute to semi-dilute concentration regime in a parallel disk and Couette flow geometry. Their results showed that the final average orientation angle of particles is not exactly in the flow direction reaching a minimum of 18° at the high $\overline{\mathrm{Pe}}$ (>100) region.

Shifting from one-dimensional (1D) flow to more complex two-dimensional (2D) flows, such as those observed in rectangular microchannels, a velocity gradient is present in both the width and thickness of the channel. Kaya and Koser[28] studied the motility of non-flagellated Escherichia *coli* bacteria (rod shape) dispersed in a mixture of Luria–Bertani broth and glycerol by pumping it into a rectangular microchannel. At a constant shear rate, the effect of aspect ratio and distance to the wall affected the motion of bacteria cells which displayed closed Jeffery orbits near the surface. These cells tended to do kayaking motions and pass through an orientation parallel to the bottom surface of the channel. Zottl *et al.*[43] studied the effect of particle size and the flow shear rate in the dilute colloidal system of silica Brownian particles to understand the orientational dynamics of heavy silica rods sheared under Poiseuille flow in a rectangular channel.

They demonstrated for rods of lengths of a few micrometers ($<30\,\mu$m), for both groups of the small particle length and the low shear rate, the system's dynamics are governed by rotational Brownian motion, while for high shear rates or long particles, dynamics depend essentially on the competition between Jeffery rotation (in the xz plane) and Brownian fluctuations which cause fast deviation from Jeffery's motion. This competition leads to an aperiodicity of particle's motion containing jumping between Jeffery orbits with different constant values, stochastic kayaking motion, and in-plane tumbling motion (in the xy plane) which is not predicted by Jeffery theory.

Rheological measurements have also been performed in parallel to understand the effect of size polydispersity on the evolution of suspensions microstructure. Lang and Lettinga[10] showed that in a mixture of bi-disperse high aspect ratio rods, the rheological response can be dominated by either the longer species or the average particle length depending on the $\overline{\mathrm{Pe}}$ range. The shear flow behavior of semi-dilute system was also explored for a bi-disperse mixture of fd-virus with two distinct lengths. In a constant total volume fraction of particles, by changing the ratio of shorter particles to longer ones, the shear viscosity was measured vs the applied shear rate. The shear-thinning parameter was reported to change almost linearly with the mixing parameter. While this behavior was dominated mainly by the alignment of the longer species, the zero-shear viscosity showed a clear non-linear trend, implying that both species contributed to rotational hindrance.

In the previous studies, most of the works have been devoted to understanding the behavior of the individual particles with moderate aspect ratios or the suspension of particles with low polydispersity in size. Although there are a few studies on high aspect ratio and polydisperse carbon nanoparticle systems, a clear distinction between the effect of polydispersity vs other effects such as Brownian motion or particle interactions is still not fully explored. For polydisperse colloidal suspensions with high aspect ratios, a full analysis of the effect of external fields on the evolution of spatial and orientation PDF of particles has not been conducted. Furthermore, the previous literature has explored Jeffery motion under homogenous linear 1D flows. Although the capillary and slit dies have been extensively used to study the rheological properties of unfilled polymer melts and particle ordering, equilibrium position in a duct and cross-sectional migration in suspensions,[44–47] the ordering of high aspect ratio and polydisperse suspensions in an inhomogeneous 2D flow field which causes non-Jeffery particle motion remains to be elusive.

In this work, we present an experimental investigation of the dynamics of polydisperse anisotropic colloids in a Newtonian medium in a capillary flow. We employ a rectangular die geometry to explore their dynamics under a complex 2D flow field. The benefit of a rectangular die geometry study lies in a well-developed analysis of the simple flow behavior in each flow layer in comparison to capillary rheometry with a circular cross-section or a Couette geometry with a curved surface and end effect issue.[4,48,49] SALS is employed to characterize *in situ* the evolution of the microstructure during flow. SALS offers a simple, fast, and precise method for the determination of behavior of particles in nanomaterials. It can provide information on particles' ensembles, fractal dimensions, and large agglomerations which are representative of real suspensions in the environment and industries.[50] Moreover, SALS can capture microstructural changes either due to concentration fluctuations or because of the orientation fluctuations.[13,51] Two types of particles are chosen with similar average lengths, but different shapes which result in different aspect ratios to investigate their microstructural evolution in the capillary flow. Specifically, we show that due to the polydispersity of the particles' fractals, an in-plane rotational motion of particles occurs followed by orientational phase mixing and demixing during flow. The analysis is conducted as a function of particle concentration and average Peclet numbers.

EXPERIMENTAL

Materials and preparation of suspensions

The Newtonian fluid used in this investigation is a mixture of 86.5 wt. % of glycerol ($\geq$ 99.0%) and de-ionized (DI) water. The density of the fluid is 1.22 g/ml, and the viscosity is 0.18 Pa s at 20 °C. Two kinds of nanoparticles were dispersed in the medium: titania and kaolinite. All the materials were purchased from Sigma-Aldrich. Suspensions of each of the particles were prepared by an ultrasonic probe sonicator (Qsonica sonicator 125 W). The mass of particles was chosen in a way that, at the end, the volume fraction of particles in the medium was based on Table I, and the medium contains 86.5 wt. % glycerol and 13.5 wt. % water with a refractive index of 1.47. For each sample, the particle is added to water and sonicated for 5 min with 50% amplitude using the probe sonicator, while the temperature of the suspension was kept constant at room temperature with the help of a water bath. Then, glycerol was added in two halves separated by 2-h mixing step on a stirrer. The suspension was then stirred for 22 h at room temperature and a speed of 700 rpm. Suspensions were passed through a 40 μm paper filter to eliminate any large agglomerates before starting rheological measurements or pumping through a macrofluidic/SALS setup. The best dispersion level obtained without damaging the particles presented individual particles as well as stable particles' bundles in the case of titania and flake-like stacks in the case of kaolinite ($\rho_{\mathrm{Ti}} = 3.8$ and $\rho_{\mathrm{KLT}} = 2.4\,{}^{\mathrm{gr}}/_{\mathrm{cm}^3}$). These fractals of particles are in the scattering q-range of our setup as well as they are visible through optical microscopy. Titania rod-like particle bundles (Ti), titanium (IV) oxide, have an average length of 3.72 μm and an average aspect ratio of around 60. Nanoclay kaolinite (KLT) platelet flakes have an average length of 1.67 μm and an average aspect ratio of around 35. The distribution frequency of particle lengths is shown in Fig. 1. SEM images were taken using the FEI Quanta 250 FEG Field Emission Scanning Electron Microscope.

To prove that the fractals do not break down or develop in the shear rates experimentally probed, suspensions were subjected to more intense conditions such as applying 15-min ultrasonication time instead of 5 min, and then under flow at Pe higher than our experimental Pe values (Pe > 500). Results are reported in Fig. S1 of the supplementary material. Micrographs of the suspensions before and after

TABLE I. Names and volume fractions of analyzed suspensions.

Sample	% $\varphi_{\mathrm{dilute}}$	% φ dilute to semi-dilute transition	% $\varphi_{\mathrm{semi-dilute}}$	% φ semi-dilute to concentrated transition
Titania	1.5×10^{-3}	7.9×10^{-3}	1.5×10^{-2}	7.9×10^{-1}
Clay kaolinite	2×10^{-2}	2.3×10^{-2}	1.6×10^{-1}	2.3×10^{-1}

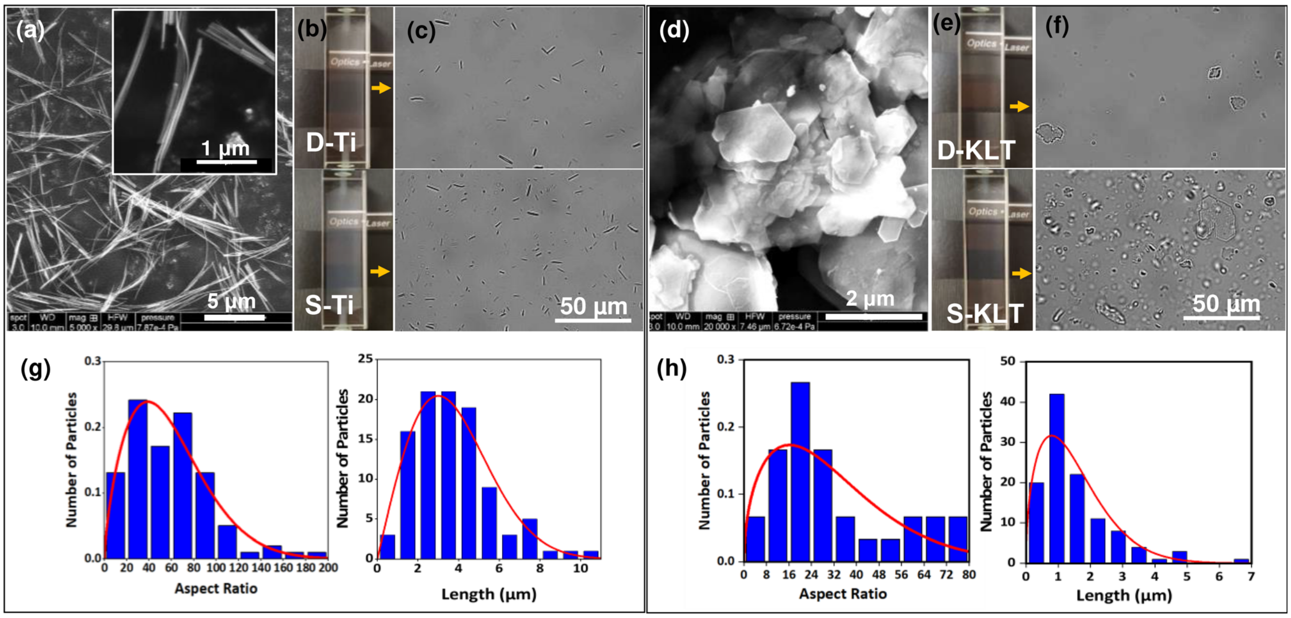

FIG. 1. Scanning electron microscopy images (a) and (d), suspension samples in the cuvette cell (b) and (e), microscopy images of suspensions (c) and (f) of titania and nanoclay kaolinite, respectively, along with their aspect ratio and size distribution diagrams (g) and (h).

sonication and before and after high Pe flow are indistinguishable which confirms that the fractals behave as solid particles in our study.

Suspension's volume fraction is calculated with the help of the particle fractal's average aspect ratio. The concentration transition from dilute to semi-dilute occurs at $\varphi_{d-s} = 1/r_a^2$ and from semi-dilute to concentrated regimes occurs at $\varphi_{s-c} = 1/r_a$, where r_a is the aspect ratio of particles and φ is the volume of a particle over the total volume of suspension. The aspect ratios used to calculate the boundaries of the regimes are the average aspect ratios.[12] The concentration regimes of the samples are reported in Table I.

Small-angle light scattering (SALS)

To study the evolution of microstructure in suspensions of non-spherical fractals, a homemade SALS setup connected to a micro-syringe pump was developed. The components of the SALS setup are shown in Figs. 2(a) and 2(b). A combination of polarizers, beam stoppers, pinholes, neutral density filters, prism, two-half convex lenses, and one achromatic lens was used to focus the scattering pattern onto a charge-coupled device, CCD camera (Thorlabs, DCC1645C-USB 2.0 CMOS Camera, 1280 × 1024) with a resolution of 3.6 μm/pixel. Thus, the intensity pattern of the scattered light can be obtained as a function of the scattering vector; $0.25 < q = 4\pi n \sin\left(\frac{\chi}{2}\right)/\lambda < 0.86\ \mu\mathrm{m}^{-1}$ corresponding with a d-spacing of approximately $7 < d < 25\ \mu$m (see Fig. S2 in the supplementary material for calibration images). The preliminary SALS tests were done on monodisperse polystyrene spherical particles with an average diameter of 8 μm to verify the q range obtained experimentally (see Fig. S3 in the supplementary material) Fig. S2. The size of the particle's agglomerates is characterized via SALS. Based on the Guinier plot (see Fig. S4 in the supplementary material), the average gyration radius is about 7.21 μm for Ti and 6.67 μm for KLT clay, respectively. These sizes are also in the scattering q-range of the SALS setup.

A rectangular quartz flow cuvette cell [see Fig. 2(c)] with inside dimensions of 2 × 35 × 10 mm and entrance and output part with an angle to minimize entrance- or end-effects [see Fig. 1(b)], purchased from Fireflysci connected to a micro-syringe pump (KD-Scientific), is coupled with the SALS setup to measure time-dependent small-angle scattering. A beam of polarized laser light from a He–Ne laser with the wavelength of 632.8 nm (Thorlabs, HNL008RB) is directed through the sample along the z direction. The path length of the beam is 2 mm.

In multicomponent systems, one can take advantage of anisotropy in refractive indices of components and study the dynamics of individual constituents. When light passes through a suspension, some part of it will be scattered by particles and the medium. The suspension's refractive index tensor ($\mathbf{n}$) can be affected by an orienting field. Measuring the differences in principal eigenvalues of the particle's refractive index will contribute to optical anisotropies of the system. Therefore, in a system of particles dispersed in a medium, a concise way to capture the average orientation of the particles can be defined by the ensemble average of the dyadic product $\langle \mathbf{pp} \rangle$, where $\mathbf{p}$ is the unit vector characterizing the orientation of each particle.[52,53] Similarly, in SALS 2D patterns or in the reciprocal space, a measure of the degree of particle alignment is defined by $\langle \mathbf{qq} \rangle$ which is the ensemble average of the dyadic product of the scattering vector $\mathbf{q}$. From this, the anisotropy factor (AF) and the average orientation angle (χ) are obtained as below,[11]

$$\mathrm{AF} = \sqrt{\frac{\left(\langle \mathbf{qq} \rangle_{xx} - \langle \mathbf{qq} \rangle_{yy}\right)^2 + 4\langle \mathbf{qq} \rangle_{xy}^{\,2}}{S}}, \tag{1}$$

$$\chi = 0.5 \tan^{-1} \frac{2\langle \mathbf{qq} \rangle_{xy}}{\langle \mathbf{qq} \rangle_{xx} - \langle \mathbf{qq} \rangle_{yy}}, \tag{2}$$

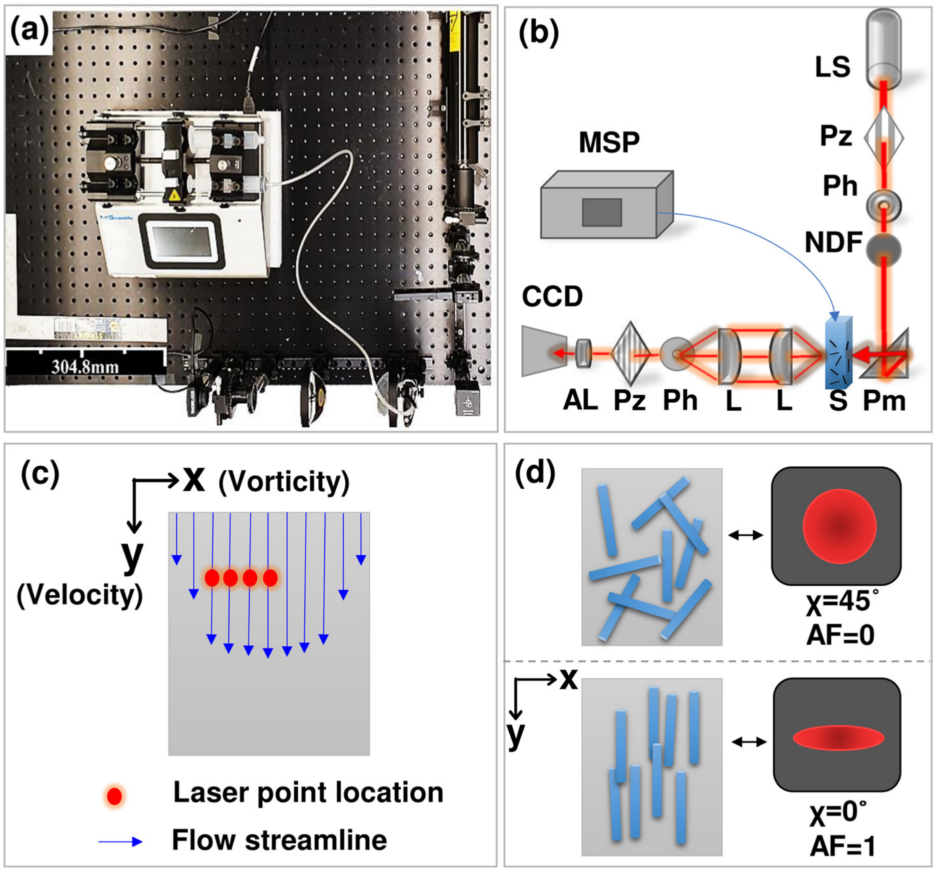

FIG. 2. (a) Small-angle light scattering (SALS) apparatus and (b) schematic of SALS setup. The components include light source (LS), polarizer (Pz), pinhole (Ph), neutral density filter (NDF), prism (Pm), sample (S), curved lens (L), achromatic lens (AL), camera (CCD), and micro-syringe pump (MSP). (c) Coordinate system and locations of laser (red points) on the flow cuvette cell (gray rectangle). (d) Representation of the scattering pattern on CCD screen (black square) related to isotropic (up) and fully anisotropic (down) distribution of particles in the cuvette cell.

where, along a circumference, $\mathrm{S}=\int_0^{2\pi}\mathrm{I}_\vartheta \mathrm{d}\vartheta$, $\mathbf{q}_\mathrm{x} = \cos\vartheta$, $\mathbf{q}_\mathrm{y} = \sin\vartheta$, $\langle\mathbf{qq}\rangle_\mathrm{xx} = \int_0^{2\pi}[(\cos\vartheta)^2\mathrm{I}_\vartheta \mathrm{d}\vartheta]/\mathrm{S}$, $\langle\mathbf{qq}\rangle_\mathrm{yy} = \int_0^{2\pi}[(\sin\vartheta)^2\mathrm{I}_\vartheta \mathrm{d}\vartheta]/\mathrm{S}$, and $\langle\mathbf{qq}\rangle_\mathrm{xy} = \int_0^{2\pi}[\cos\vartheta\sin\vartheta\mathrm{I}_\vartheta \mathrm{d}\vartheta]/\mathrm{S}$, and I_ϑ is the value of intensity at the location (r, ϑ) of the SALS 2D pattern. The AF shows the scattering anisotropy and defines the degree of spreading of orientation in the suspension, while χ quantifies the average orientation angle with respect to the flow direction.

To relate the orientation distribution to the SALS profiles of a system where the particle size is larger than the wavelength of the light source, diffraction theory for dilute suspensions of very large particles is used, as in the work of Salem and Fuller.[13] It is assumed that each particle scatters the light individually and multiple scattering is negligible. Therefore, the final scattering pattern results in the superposition of scattering patterns from each particle with a distinct orientation.

To investigate the effects of applied shear rate on particle fractals at different positions of the flow, a rectangular capillary geometry with a thickness-to-width ratio equal to 2:10 is chosen. Salek and Martinuzzi[54] simulated the velocity profiles in a flow cell with the same aspect ratio. They depicted the velocity profiles in both width and thickness dimensions of the cell and found that, far from the walls, the slope of the velocity profile in the thickness of the cell is less than the one in the width of the cell.

Two sets of experiments are designed. In the first sets of experiments, the laser point is fixed at a location of the cuvette and the flow shear rate is changed with the help of the micro-syringe pump. The fixed laser location is at the centerline of the cuvette and at a vertical distance of 2.5 cm from where the flow is fully developed. This fixed laser point is used in all the experiments presented in this work. To estimate the average shear rate at each point of the cuvette, we calculate the velocity profile in the xy plane of the cuvette by the help of COMSOL (see Table SI and Fig. S5 in the supplementary material). The strain and the maximum strain applied on the suspensions were calculated by the help of the average shear rate and are shown in the following figures by a vertical dashed line (i.e., Figs. 4 and 7). Such strain is not a pure deformation because of the non-homogenous nature of the flow, but it is useful here to compare data at different Pe numbers.

In the second set of experiment, the local shear rate of the capillary flow is fixed at a value by fixing the volumetric flow rate of the micro-syringe pump. The lateral position of the laser is changed on the cuvette moving from the centerline toward the lateral wall of the cuvette, perpendicular to the flow direction. In this case, we named the test done at the centerline as the "0 mm" test and a test performed 3 mm away from the centerline as the "3 mm" test. In the latter series of tests, the effect of cross migration of particles was investigated as well. No migration was observed in our experiments confirming negligible secondary flows due to the low concentrations explored. This is shown in Fig. S6 in the supplementary material, where the total intensity is basically constant with changing the position of the laser.

RESULTS AND DISCUSSION

Viscosity measurements

To study the rheological behavior of samples, an Anton-Paar rheometer (MCR 702) equipped with concentric cylinder geometry (Bob-CC20 outer diameter 20 mm and CupC-CC20 inner diameter 22 mm) was used. The samples were pre-sheared at a shear rate of 10 s^{-1} for 1 min and then allowed to rest for 15 min to cancel possible effects of loading. A constant shear rate was applied at each step in the range of 0.1–500 s^{-1}, and viscosity was measured as a function of the shear rate. All samples show a Newtonian behavior in the range of shear rates explored. Figure S7 shows Newtonian behavior for semi-dilute samples, while qualitatively similar curves were obtained for the dilute samples (not reported).

Equilibrium scattering patterns of dilute suspensions

The steady-state SALS data at rest (no flow) for dispersions of Ti and KLT at the dilute concentration regime are shown in Fig. 3 as a function of the scattering vector (q). In the range $qa \gg 1$, where a is the larger dimension of a particle, the scattered intensity for both systems shows a power law decay of $I(q) \propto q^{-d_f}$, where d_f represents the form factor of the particle which scattered the light or the fractal dimension here.[8,55–57] Figure 3 shows a $d_f = 1.2$ for Ti particle and a $d_f = 1.9$ for KLT fractals in accord with the expected fractal dimension for a rod-like bundle ($d_f = 1$) and a platelet flake ($d_f = 2$).[8,58] The slight deviation from the expected values is expected due to the polydispersity of the samples.

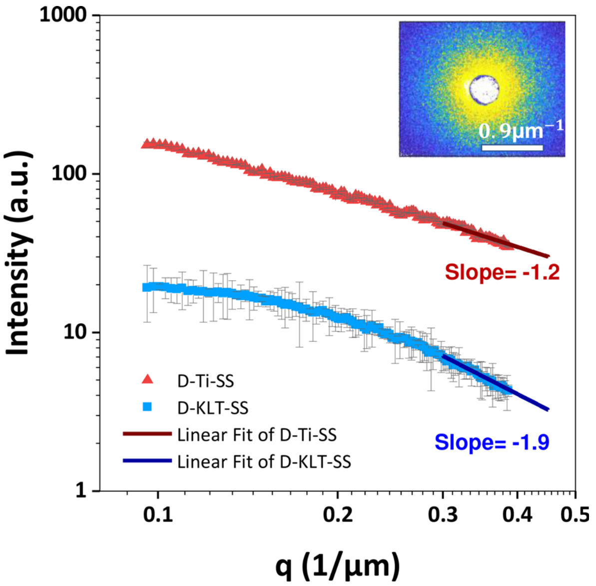

FIG. 3. Angular averaged scattering intensity as a function of scattering vector for dilute suspensions of D-Ti and D-KLT (intensity × 10^1) at rest mode ($\dot{\gamma} = 0$) extracted from the related 2D scattering pattern in the xy plane. The R^2 value for all diagrams is larger than 0.9.

Transient response under capillary flow

Dilute and semi-dilute suspensions of rod-like and platelet fractals were subjected to a capillary flow, which results are illustrated in Figs. 4–8 for both particle fractals at different shear rates [$\overline{Pe} \approx O(0.1)$ to O(100)].

Dynamics of dilute suspensions

The anisotropy factor (AF) and the average orientation angle (χ) of the dilute suspensions as a function of applied strain are illustrated in Fig. 4. Probing at a fixed position on the centerline of the cuvette, particles' AF is measured vs applied strain. Before the shear is applied (strain = 0), a negligible AF is obtained with an isotropic orientation angle (± 45°) due to the random orientation of particles. By applying a startup flow, particles in a monodisperse system will tumble indefinitely with time at high $\overline{Pe}$ in Jeffery orbits.[59] In a polydisperse system, due to the distribution of angular velocities of the particles, the scattering will show first an increase in AF and a decrease in χ with strain due to the orientational phase mixing of the particles.[35] Particles with larger aspect ratios are tumbling slower than the smaller aspect ratios particles which lead to a loss in the correlation between particles' orientation dynamics. Figures 4(a) and 4(c) show the results for Ti bundles where, at low $\overline{Pe}$ (<1), the AF reaches a maximum value, AF ≈ 0.6, where bundles are aligned within flow direction, $-5° < \chi < 5°$, and no further changes are observed in AF by increasing the strain. While for higher values of $\overline{Pe}$ (>1), the AF first increases to higher peak values with increasing the $\overline{Pe}$ and then decreases. This decrease cannot be attributed to the flocs' breakdown because the break-up of flocs would decrease the radius of gyration obtained during SALS which was not observed in any of the suspensions here investigated. (Guinier plots are not given here since no specific changes were seen.)[3–5] Figure S8 in the supplementary material shows the total intensity as a function of strain for D-Ti at the highest shear regime near the wall of the cuvette cell (3 mm). The decrease in AF is caused by the orientational phase demixing of the particles. This behavior agrees well with the observations by Salem and Fuller[13] in simple shear flow on the dilute system of prolate hardened human red blood cells. By applying flow in a parallel plate device, they observed a peak in the degree of anisotropy at low particle's Re (≈ 0.005) and high $\overline{Pe}$ (10^4) numbers. However, the transient evolution of the microstructure was not demonstrated during startup flow.

Similar measurements made with KLT platelets resulted in a qualitatively similar trend of AF but, very different behavior of χ, shown in Figs. 4(c) and 4(d), respectively. Although the AF increases to almost half of the value of rod-like Ti, AF ≈ 0.4, the average orientation angle of bundles moves periodically up and down around 0° in an almost symmetrical way about the flow direction in the shear plane[60] and over a large range ($-25° < \chi < 25°$) even for the highest $\overline{Pe}$ value. This shows that the KLT platelets present a wagging dynamic in the capillary flow field, not present in the Ti rod-like bundles, because of the two-dimensional shape and smaller aspect ratio. These data are consistent with Reddy's[36] work on gold non-spherical nanoparticles, where the dichroism and χ exhibited an increasing and decreasing trend at Pe < 1. For Pe > 1, χ eventually reached a value around 0° relative to the flow direction and dichroism increased for about one order of magnitude. Xie *et al.*[61] also worked on the flow-induced alignment of gold nanorods with low to moderate aspect ratios in the range of 2.4–4.2 in an aqueous suspension by the help of dichroism and in a

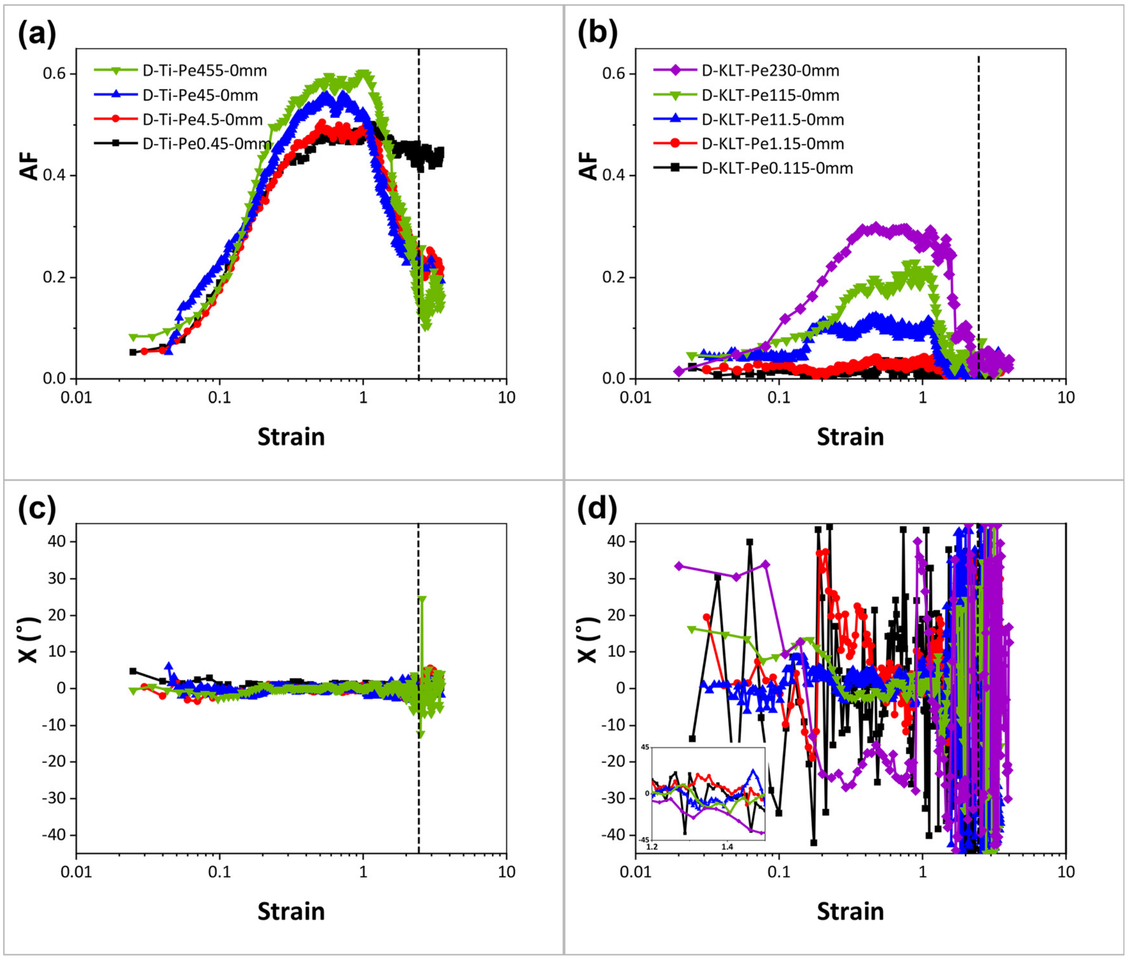

FIG. 4. Anisotropy factor and average orientation angle as a function of strain for D-Ti suspension (a) and (c) and D-KLT suspension (b) and (d) at different $\overline{\mathrm{Pe}}$ numbers and at the cuvette centerline (0 mm). The diagram (d) contains an inset of average angle between the strain of 1.2–1.5 in linear scale.

Couette geometry. They reported that low aspect ratio rods tend to flip between two extreme orientations of the Jeffery orbits which illustrate the strong effect of Brownian motion even at high $\overline{\mathrm{Pe}}$ (>200) numbers where the highest particle alignment happened.

Spatial changes in microstructures under capillary flow

Moving from the centerline of the cuvette toward the lateral wall [as shown in Fig. 2(c)], the local $\overline{\mathrm{Pe}}$ of flow changes due to the shear rate gradient present in the capillary flow in the vorticity direction. The polydispersity in the shear rate is investigated through the COMSOL-evaluated velocity and shear rate profiles. The shear rate deviation from the averaged shear rate is presented in Fig. S9 and Table SII in the supplementary material for each point of laser under study. There is also a gradient in shear across the thickness of the cuvette (z), and an average over the shear rate in this direction is calculated to consider this effect.

Figures 5(a) and 5(b) show AF vs strain for fractals at different positions relative to the cuvette centerline. Moving away from the cuvette centerline in the x direction, Fig. 5(a) presents a marked increase in the terminal part of AF due to the larger shear rates approaching the wall. A similar trend is also found in Fig. 5(b) for KLT, which also shows an overshoot in all curves.

Looking into the details of the SALS pattern helps further improve the understanding of the particles' dynamics. At the highest shear rate ($\overline{\mathrm{Pe}} = 455$ for Ti and $\overline{\mathrm{Pe}} = 115$ for KLT clay), the time sequence of contours of the SALS pattern was extracted at the centerline of the cuvette (0 mm) as illustrated in Figs. 5(c) and 5(d). At rest, Figs. 5(c-i) and 5(d-i), both suspensions show a circularly symmetric pattern related to the isotropic state of the particles. As the suspension is subjected to the flow, patterns undergo remarkable changes, Figs. 5(c-ii) and 5(c-iii). The SALS profiles become monomodal elliptical with their long axis oriented in the x direction containing a strong equatorial streak, meaning rod-like bundles are oriented toward the flow (y) direction. After passing the plateau of the position (iii), the orientational phase demixing of bundles with different aspect ratios result in a transformation from an elliptical pattern to a diamond-like pattern. The polydispersity

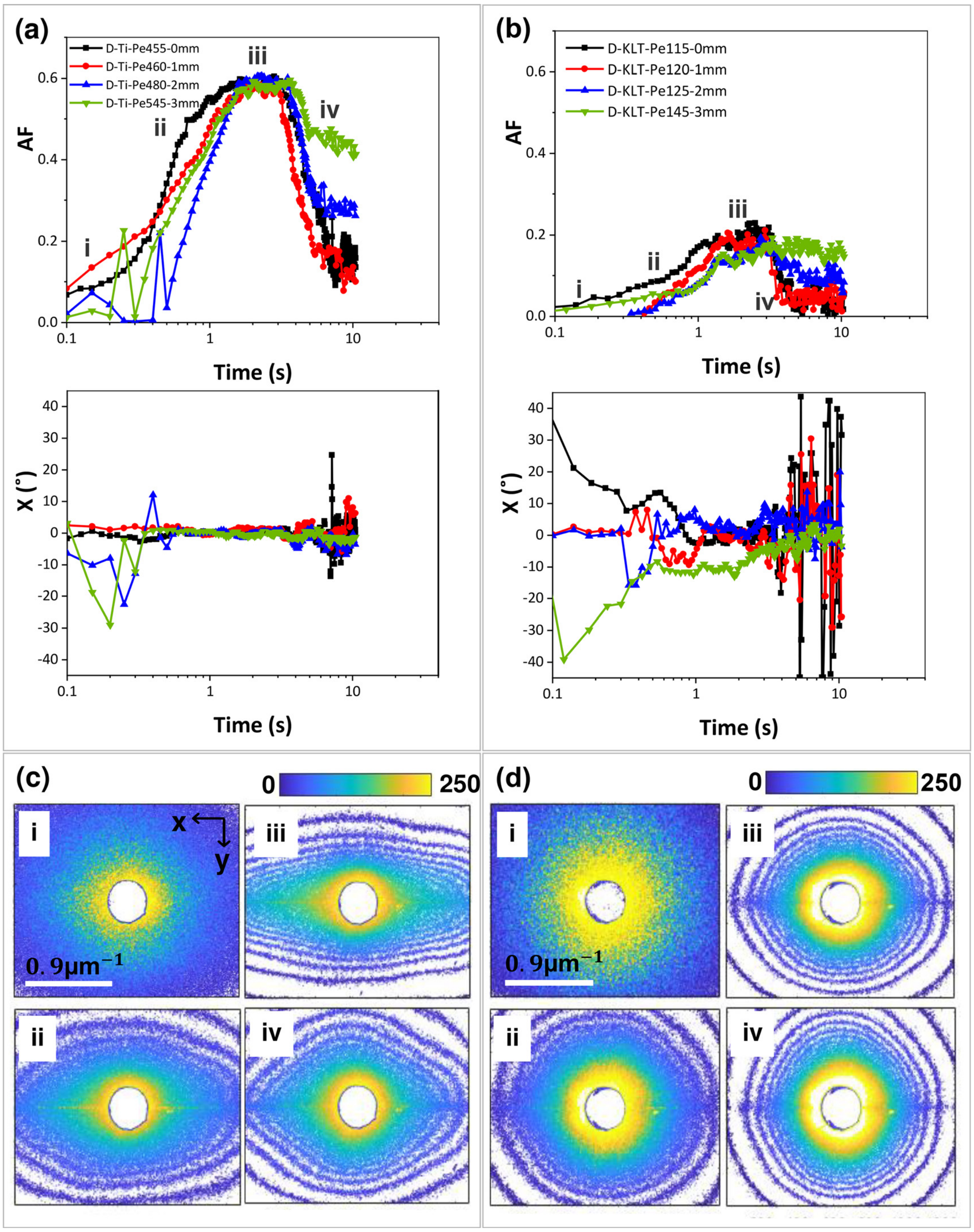

FIG. 5. Anisotropy factor as a function of time and its relative contours for D-Ti suspension (a) and (c) and D-KLT suspension (b) and (d) at different laser positions (0, 1, 2, and 3 mm) of the cuvette cell.

of fractals and the gradient in shear rate across the cuvette cell cause various periods of rotation[62] which result in the damping of oscillations, in agreement with the previous measurements of Johnson *et al.*,[11] Salem and Fuller,[13] and Stover and Cohen[18] on biaxial particles.

Similar patterns are illustrated for KLT in Figs. 5(b) and 5(d). Although the total trend of AF is qualitatively similar to that of Ti rods, distinct features can be seen in these patterns. The clay platelets' maximum AF is always less than the value of Ti rods (see Fig. 4 for comparison at different $\overline{\mathrm{Pe}}$ numbers) which shows that a fewer

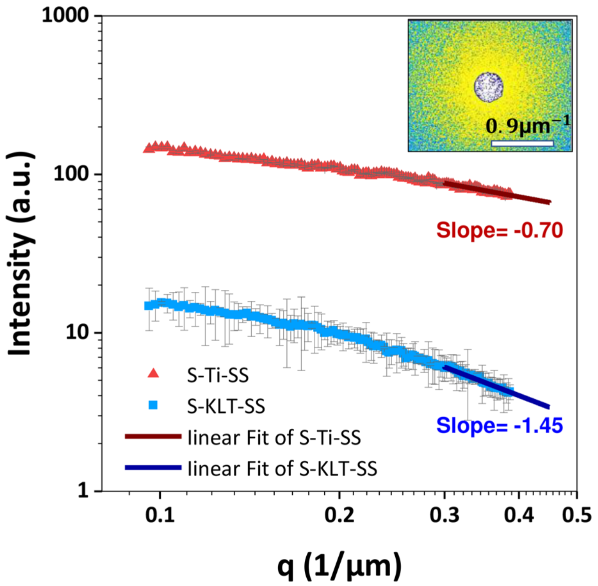

FIG. 6. Angular averaged scattering intensity as a function of scattering vector for semi-dilute suspensions of S-Ti and S-KLT (intensity × 10^1) at rest mode ($\dot{\gamma}$ =0) extracted from the related 2D scattering pattern in the xy plane. The R^2 value for all diagrams is larger than 0.9.

number of the platelets tend to align in the flow direction in comparison with the rods. Also, the SALS contours for KLT are slightly changing their shapes from a circular symmetric profile in Fig. 5(d-i) to a slightly elliptical shape with its longer axes in the x direction and then in the flow direction, in Figs. 5(d-iii) and 5(d-iv), respectively. Similar behavior was shown in the work of Fry *et al.*[41] where multi-walled carbon nanotubes in bulk show less alignment along the flow direction than particles close to the shearing surface.

Equilibrium scattering patterns of semi-dilute suspensions

By varying the concentration from dilute to semi-dilute concentration regime under static conditions, the intensity for both systems increases similarly, while their slope with respect to q is decreased and this is indicated in Fig. 6. This feature arises from interference effects due to increasing particle–particle (e.g., fractal–fractal) interaction which results in the higher ordering of fractals. This feature is more pronounced at lower q range ($<0.17\ \mu m^{-1}$) where the short-range ordering of particles produces a more marked decrease in intensity. This is in agreement with the work of Ramsay and Lindner[58] who investigated the structure of montmorillonite clay colloidal suspensions with the help of SANS as well as other reports on oxide sols[63] and latex systems[64] where repulsive interactions between particles due to electric double layer promote the short-range ordering in the system.[58]

Dynamics of semi-dilute suspensions

Figure 7 shows the effect of capillary flow on the evolution of microstructure for samples in a semi-dilute regime. Compared to Fig. 4 of dilute samples, the AF of the semi-dilute systems has a lower value than in dilute systems, and the χ of semi-dilute samples fluctuates in a smaller range due to the hydrodynamic interactions and excluded volume hindrance.[4,10] This behavior was also observed in an earlier investigation of Hilliou *et al.*[65] on hairy-rod polymer in simple shear flow. They found that the trimers in the dilute system orient along the flow direction. But in a semi-dilute system, a second population of larger (in terms of aspect ratio) associations form which tend to orient in the vorticity direction with their constituent chains in the flow direction.

Moreover, for both rod-like and platelet fractals, the damping behavior is obvious in AF and χ diagrams even at the lowest $\overline{\text{Pe}}$ (<1). The AF diagram of the highest $\overline{\text{Pe}}$ (445 and 230 for semi-dilute Ti and KLT, respectively) is split into six regions to study the microstructure with the help of SALS contours in Figs. 7(c) and 7(d). The circular pattern of the static condition is nearly unchanged, with a higher value of intensity due to the higher concentration of the system. This is consistent with the work of Fry *et al.*[41] on the carbon nanotubes where the scattering anisotropy for the dilute regime of single-walled nanotubes is smaller than the semi-dilute regime of multi-walled nanotubes, especially in the low-scattering vector region. Moreover, the increase in intensity is not linear especially at the highest shear rate which is a consequence of the hydrodynamic interactions between particles.[8] By increasing the strain on rod-like bundles, an equatorial streak shapes in the middle of the circular pattern in Fig. 7(c-ii) which then transform into a butterfly pattern with two lobes at higher strains in Fig. 7(c-iii). It is noteworthy that the butterfly pattern is stretched in the x direction up to the region Fig. 7(c-iv) and then changes to a nearly circular pattern at higher strains due to the orientational demixing of the particle fractals in Figs. 7(c-v) and 7(c-vi).

In the case of KLT nanoclay, reduced fluctuations of average orientation angle (χ) are observed in Figs. 7(b-ii) and 7(b-iii) with an increase in KLT concentration. In Fig. 7(d), a monomodal pattern with a weak equatorial line is shown, and it transforms by applying strain to a two-lobes butterfly pattern at region Fig. 7(d-iii). Also, the pattern of Fig. 7(d-iii) is slightly elliptical shaped, and it is oriented in the x direction, while in Fig. 7(d-vi), it is oriented in the flow direction. These results show an evolution from alignments predominantly in the flow direction toward alignments in the x direction as the strain is increased.

This is qualitatively consistent with the work of Siddiquee and van Egmond[66] on semi-dilute solutions of stiff wormlike polymer and Lee *et al.*[67] on the dynamics of dispersions of rod-like proteins. While the smaller particles remain practically randomized at low shear rates, the larger associations orient in the flow direction since they possess a smaller rotational diffusivity which results in a larger effective shear rate experienced by this species. Enhancing the shear rate causes a cluster orientation perpendicular to the flow direction.

To understand the average orientation angle when the system is at the highest level of particle ordering, the data on average AF and χ vs $\overline{\text{Pe}}$ at the peak of AF for both rod-like and platelet fractals in dilute and semi-dilute regimes are shown in Fig. 8 at two different positions on the flow cell (see Figs. S10 and S11 in the supplementary material for data on all samples). Figures 8(a) and 8(b) show that the AF of rod-like Ti bundles is higher than platelet clay flakes in both concentration regimes. Figures 8(c) and 8(d) show their relative average orientation angle, respectively. Ti rod-like bundles show an average orientation angle around 0 relative to the flow direction and show a

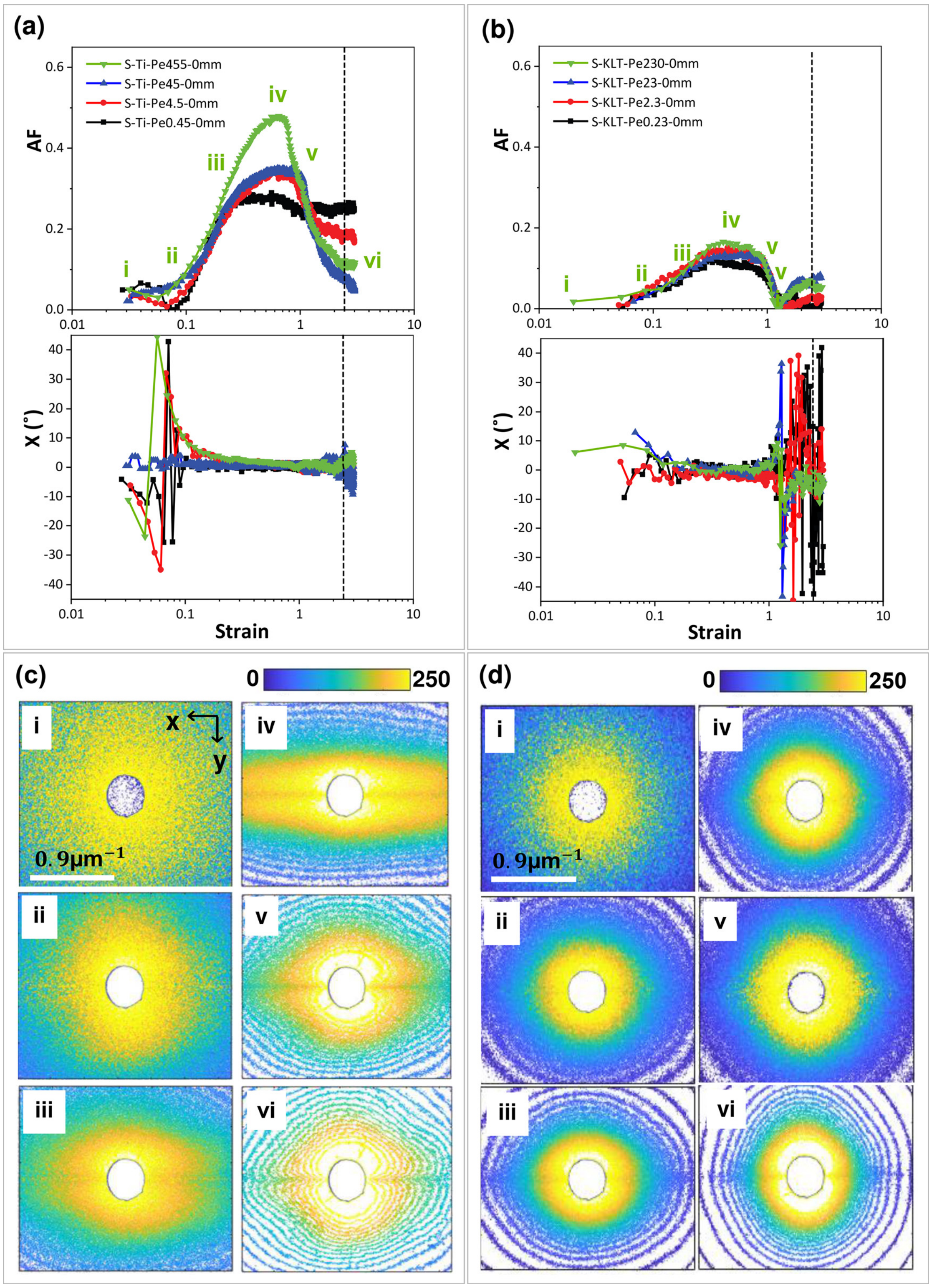

FIG. 7. Anisotropy factor as a function of Pe according with its average orientation angle (a), and its relative SALS contours for S-Ti suspension (c); the same diagrams of AF, χ, and SALS contours for S-KLT suspension (b) and (d) at the cuvette centerline (0 mm). Symbols and the corresponding sample names are given in (a) and (b).

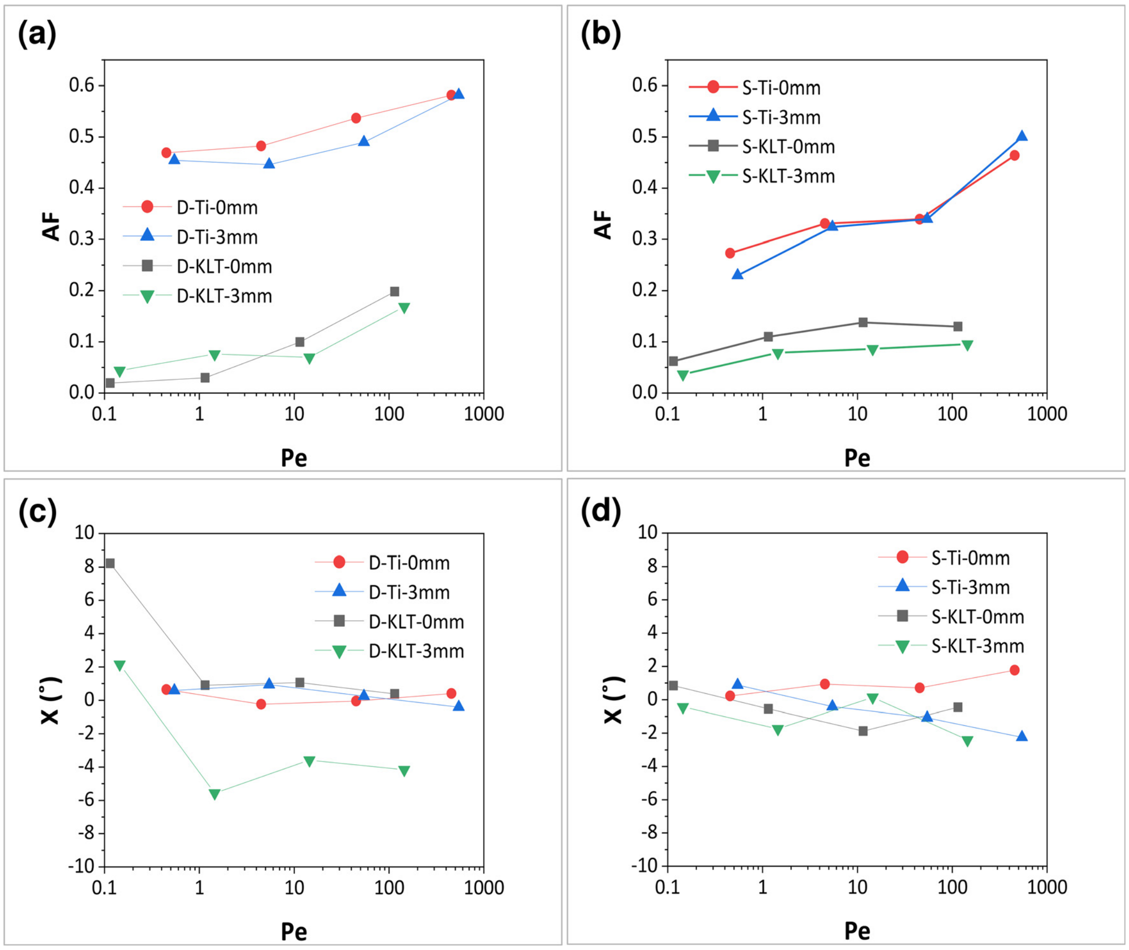

FIG. 8. Anisotropy factor and the relative average orientation angle as a function of $\overline{\mathrm{Pe}}$ for dilute suspensions (a) and (b) and semi-dilute suspensions (c) and (d) at different laser positions (0 and 3 mm) of the cuvette cell. Lines are guide for the eyes.

slight deviation from zero at high $\overline{\mathrm{Pe}}$ numbers in the semi-dilute regime. In contrast, KLT platelets show an overall more isotropic behavior in particular, at low $\overline{\mathrm{Pe}}$ (< 1), which changes to a wagging dynamic at higher Pe. Increasing the distance from the cuvette centerline to 3 mm position corresponds to a change in the χ from 0° to around $-5°$. While this variation is limited to ±3° in the semi-dilute concentration.

Egres *et al.*[68] performed Rheo-SANS investigations of acicular (needle-shaped) calcium carbonate colloidal suspensions. They showed in the dilute regime, the order parameter of particles with an aspect ratio ranging from 2 to 7 increases with increasing $\overline{\mathrm{Pe}}$ from almost 30 to 10^4. While for more concentrated suspensions, a decrease in order parameter was shown because of forming hydro-clusters and shear thickening behavior of the system. Considering the above-mentioned effects of particles' aspect ratio,[66,67] it can be also concluded that the higher AF of Ti bundles may relate to their higher aspect ratio in comparison to the KLT flakes. Although the average length of fractals is in the same order of magnitude, the KLT systems contain fractals with a smaller aspect ratio which can rotate rapidly even at an average $\overline{\mathrm{Pe}} < 1$ and decrease the value of AF or increase the χ. Increasing the concentration of system to the semi-dilute regime may reduce the number of fractals due to the formation of some aggregates which leads to a slight increase in AF at low $\overline{\mathrm{Pe}}$ or a χ factor close to 0°.

CONCLUSIONS

Shear-induced micro-structure of non-spherical colloidal particles possessing polydispersity in size is investigated using a high-resolution homebuilt SALS setup. SALS enabled *in situ* and real-time probing of the spatial organization and orientation dynamics of particles in dilute and semi-dilute regimes under shear flow. While the differences in rheological response are subtle, a very complex dynamics was observed in the microstructure which highlights the importance of rheo-optical measurements. The results of AF and average orientation angle measurements were critically compared for Ti rod-like and KLT platelet fractals. In the dilute regime, the equilibrium (at $\dot{\gamma} = 0\,\mathrm{s}^{-1}$) diagram of I − q shows a slope of (-1.2) for rods and (-1.9) for platelets illustrating fractals are polydisperse in these systems compared to non-colloidal monodisperse suspensions of rods (-1) and platelets (-2).

Capillary flow with a rectangular cross-section is used in light scattering studies to explore the effects of shear rate spatial gradient on the suspensions' microstructure. Polydisperse fractals with a high aspect ratio are used. We found that particles become partially aligned along the flow direction even at $\overline{\mathrm{Pe}} < 0.5$ for rods and at $\overline{\mathrm{Pe}} \gtrsim 10$ for platelets due to hydrodynamic forces. Platelets exhibit a wagging dynamic in the xy plane which was not observed with the rod counterpart.

The polydisperse particle fractals show a rapid damping behavior after a large peak of AF. In contrast to the nearly circular SALS pattern of wagging platelets, rods show a clear ellipsoidal pattern when phase mixing occurs, followed by a diamond shape pattern due to the orientational phase demixing of the particle fractals.[13]

We also demonstrated the effect of the shear rate gradient in the vorticity direction of a rectangular capillary flow by shifting the laser location point toward the lateral wall. In the absence of any secondary flow, by moving closer to the wall of the cuvette, the platelet fractals show a deviation of about 6° in χ, while rods tend to show a higher alignment toward the flow direction.

In the semi-dilute regime of concentration, particle fractals show ordering even at rest due to the short-range electrostatic particle–particle (fractal–fractal) interactions. Both particle fractals show a lower anisotropy factor compared to the dilute regime case, while the χ is slightly deviating from the flow direction.

The flow-induced microstructures observed in this work provides details in controlling anisotropic colloidal suspensions. Benefitting from the 2D nature of the capillary flow, the reported details can guide the design of processing schemes to produce engineering nanomaterials with anisotropic properties such as barriers and membranes[69–72] and nanocomposite hydrogels for tissue engineering and biomedical applications.[6,73–75]

SUPPLEMENTARY MATERIAL

See the supplementary material for data-reporting microscopy micrographs, SALS calibration, anisotropy factor, orientation angle, and total intensity vs Pe number as well as numerical simulation results.

ACKNOWLEDGMENTS

G.N., R.S., and N.M. gratefully acknowledge the financial support provided by the American Chemical Society's Petroleum Research Fund (ACS) and The Natural Sciences and Engineering Research Council of Canada (NSERC) at the University of Calgary.

AUTHOR DECLARATIONS

Conflict of Interest

The authors have no conflicts to disclose.

Author Contributions

Narges Mohammad Mehdipour: Conceptualization (equal), Data curation (equal), Formal analysis (equal), Methodology (equal), and Writing – original draft (equal). **Naveen Reddy:** Methodology (equal) and Writing – review and editing (equal). **Roman Shor:** Funding acquisition (equal), Supervision (equal), and Writing – review and editing (equal). **Giovanniantonio Natale:** Conceptualization (equal), Funding acquisition (equal), Methodology (equal), Supervision (equal), and Writing – review and editing (equal).

DATA AVAILABILITY

The data that support the findings of this study are available within the article and its supplementary material.

REFERENCES

[1] A. Karkooti *et al.*, "Graphene-based electro-conductive anti-fouling membranes for the treatment of oil sands produced water," Sci. Total Environ. **704**, 135365 (2020).

[2] W. Xia *et al.*, "Analysis of oil-in-water based nanolubricants with varying mass fractions of oil and TiO_2 nanoparticles," Wear **396–397**, 162–171 (2018).

[3] E. de Lucas-Gil *et al.*, "The benefits of the ZnO/clay composite formation as a promising antifungal coating for paint applications," Appl. Sci. **10**(4), 1322 (2020).

[4] X. Wang *et al.*, "High-shear-rate capillary viscometer for inkjet inks," Rev. Sci. Instrum. **81**(6), 065106 (2010).

[5] T. Dbouk *et al.*, "Shear-induced particle migration: Predictions from experimental evaluation of the particle stress tensor," J. Non-Newtonian Fluid Mech. **198**, 78–95 (2013).

[6] Z. Zhao *et al.*, "Bioinspired nanocomposite hydrogels with highly ordered structures," Adv. Mater. **29**(45), 1703045 (2017).

[7] Q. L. Zhu *et al.*, "Distributed electric field induces orientations of nanosheets to prepare hydrogels with elaborate ordered structures and programmed deformations," Adv. Mater. **32**(47), 2005567 (2020).

[8] N. K. Reddy *et al.*, "Rheo-optical analysis of functionalized graphene suspensions," Langmuir **34**(26), 7844–7851 (2018).

[9] E. K. Hobbie *et al.*, "Optical measurements of structure and orientation in sheared carbon-nanotube suspensions," Rev. Sci. Instrum. **74**(3), 1244–1250 (2003).

[10] C. Lang and M. P. Lettinga, "Shear flow behavior of bidisperse rodlike colloids," Macromolecules **53**(7), 2662–2668 (2020).

[11] S. J. Johnson, A. J. Salem, and G. G. Fuller, "Dynamics of colloidal particles in sheared, non-Newtonian fluids," J. Non-Newtonian Fluid Mech. **34**(1), 89–121 (1990).

[12] I. Marti *et al.*, "Rheology of concentrated suspensions containing mixtures of spheres and fibres," Rheol. Acta **44**(5), 502–512 (2005).

[13] A. J. Salem and G. G. Fuller, "Small angle light scattering as a probe of flow-induced particle orientation," J. Colloid Interface Sci. **108**(1), 149–157 (1985).

[14] J. Kim *et al.*, "Monitoring the orientation of rare-earth-doped nanorods for flow shear tomography," Nat. Nanotechnol. **12**(9), 914–919 (2017).

[15] J. Mewis and N. J. Wagner, *Colloidal Suspension Rheology* (Cambridge University Press, 2012).

[16] N. Mohammad Mehdipour, H. Garmabi, and S. Jamalpour, "Effect of nanosize $CaCO_3$ and nanoclay on morphology and properties of linear PP/branched PP blend foams," Polym. Compos. **40**(S1), E227–E241 (2019).

[17] G. B. Jeffery, "The motion of ellipsoidal particles immersed in a viscous fluid," Proc. R. Soc. London, Ser. A **102**(715), 161–179 (1922).

[18] C. A. Stover and C. Cohen, "The motion of rodlike particles in the pressure-driven flow between two flat plates," Rheol. Acta **29**(3), 192–203 (1990).

[19] S. Monjezi *et al.*, "The effect of weak confinement on the orientation of nanorods under shear flows," Nanomaterials **8**(3), 130 (2018).

[20] H. L. Goldsmith and S. Mason, "The microrheology of dispersions," in *Rheology* (Elsevier, 1967), pp. 85–250.

[21] E. Anczurowski and S. Mason, "The kinetics of flowing dispersions: III. Equilibrium orientations of rods and discs (experimental)," J. Colloid Interface Sci. **23**(4), 533–546 (1967).

[22] L. Leal and E. Hinch, "The effect of weak Brownian rotations on particles in shear flow," J. Fluid Mech. **46**(4), 685–703 (1971).

[23] R. Duggal and M. Pasquali, "Dynamics of individual single-walled carbon nanotubes in water by real-time visualization," Phys. Rev. Lett. **96**(24), 246104 (2006).

[24] E. Hinch and L. Leal, "The effect of Brownian motion on the rheological properties of a suspension of non-spherical particles," J. Fluid Mech. **52**(4), 683–712 (1972).

[25] A. Pal *et al.*, "Anisotropic dynamics and kinetic arrest of dense colloidal ellipsoids in the presence of an external field studied by differential dynamic microscopy," Sci. Adv. **6**(3), eaaw9733 (2020).

[26] C. A. Stover, D. L. Koch, and C. Cohen, "Observations of fibre orientation in simple shear flow of semi-dilute suspensions," J. Fluid Mech. **238**, 277–296 (1992).

[27] E.-J. Ding and C. K. Aidun, "The dynamics and scaling law for particles suspended in shear flow with inertia," J. Fluid Mech. **423**, 317–344 (2000).

[28] T. Kaya and H. Koser, "Characterization of hydrodynamic surface interactions of *Escherichia coli* cell bodies in shear flow," Phys. Rev. Lett. **103**(13), 138103 (2009).

[29] J. Einarsson *et al.*, "Tumbling of asymmetric microrods in a microchannel flow," Phys. Fluids **28**(1), 013302 (2016).

[30] P. L. Frattini and G. G. Fuller, "Rheo-optical studies of the effect of weak Brownian rotations in sheared suspensions," J. Fluid Mech. **168**, 119–150 (1986).

[31] M. J. Solomon and P. T. Spicer, "Microstructural regimes of colloidal rod suspensions, gels, and glasses," Soft Matter **6**(7), 1391–1400 (2010).

[32] A. Okagawa, R. Cox, and S. Mason, "The kinetics of flowing dispersions. VI. Transient orientation and rheological phenomena of rods and discs in shear flow," J. Colloid Interface Sci. **45**(2), 303–329 (1973).

[33] P. L. Frattini and G. G. Fuller, "The dynamics of dilute colloidal suspensions subject to time-dependent flow fields by conservative dichroism," J. Colloid Interface Sci. **100**(2), 506–518 (1984).

[34] S. J. Johnson and G. G. Fuller, "The optical anisotropy of sheared hematite suspensions," J. Colloid Interface Sci. **124**(2), 441–451 (1988).

[35] J. Vermant, H. Yang, and G. Fuller, "Rheo-optical determination of aspect ratio and polydispersity of nonspherical particles," AIChE J. **47**(4), 790–798 (2001).

[36] N. K. Reddy *et al.*, "Flow dichroism as a reliable method to measure the hydrodynamic aspect ratio of gold nanoparticles," ACS Nano **5**(6), 4935–4944 (2011).

[37] H. Brenner, "Rheology of a dilute suspension of axisymmetric Brownian particles," Int. J. Multiphase Flow **1**(2), 195–341 (1974).

[38] A. Ortega and J. Garcıa de la Torre, "Hydrodynamic properties of rodlike and disklike particles in dilute solution," J. Chem. Phys. **119**(18), 9914–9919 (2003).

[39] J. Vermant and M. Solomon, "Flow-induced structure in colloidal suspensions," J. Phys.: Condens. Matter **17**(4), R187 (2005).

[40] E. K. Hobbie *et al.*, "Orientation of carbon nanotubes in a sheared polymer melt," Phys. Fluids **15**(5), 1196–1202 (2003).

[41] D. Fry *et al.*, "Anisotropy of sheared carbon-nanotube suspensions," Phys. Rev. Lett. **95**(3), 038304 (2005).

[42] G. Natale *et al.*, "Rheo-optical response of carbon nanotube suspensions," J. Rheol. **59**(2), 499–524 (2015).

[43] A. Zöttl *et al.*, "Dynamics of individual Brownian rods in a microchannel flow," Soft Matter **15**(29), 5810–5814 (2019).

[44] J. Aho and S. Syrjälä, "Shear viscosity measurements of polymer melts using injection molding machine with adjustable slit die," Polym. Test. **30**(6), 595–601 (2011).

[45] J. Zhou and I. Papautsky, "Fundamentals of inertial focusing in microchannels," Lab Chip **13**(6), 1121–1132 (2013).

[46] B. Chun and A. Ladd, "Inertial migration of neutrally buoyant particles in a square duct: An investigation of multiple equilibrium positions," Phys. Fluids **18**(3), 031704 (2006).

[47] Y. Son, "Determination of shear viscosity and shear rate from pressure drop and flow rate relationship in a rectangular channel," Polymer **48**(2), 632–637 (2007).

[48] M. Kaseem, K. Hamad, and F. Deri, "Slit die rheology of thermoplastic starch during extrusion process," Int. J. Plast. Technol. **17**(1), 51–60 (2013).

[49] C. Han and M. Charles, "Measurement of the axial pressure distribution of molten polymers in flow through a rectangular duct," Trans. Soc. Rheol. **15**(1), 147–161 (1971).

[50] S. K. Brar and M. Verma, "Measurement of nanoparticles by light-scattering techniques," TrAC Trends Anal. Chem. **30**(1), 4–17 (2011).

[51] T. Hashimoto, T. Takebe, and S. Suehiro, "Apparatus to measure small-angle light scattering profiles of polymers under shear flow," Polym. J. **18**(2), 123–130 (1986).

[52] S. Pujari *et al.*, "Orientation dynamics in multiwalled carbon nanotube dispersions under shear flow," J. Chem. Phys. **130**(21), 214903 (2009).

[53] S. Pujari *et al.*, "Shear-induced anisotropy of concentrated multiwalled carbon nanotube suspensions using x-ray scattering," J. Rheol. **55**(5), 1033–1058 (2011).

[54] M. M. Salek and R. J. Martinuzzi, "Numerical simulation of fluid flow and hydrodynamic analysis in commonly used biomedical devices in biofilm studies," in *Numerical Simulations—Examples and Applications in Computational Fluid Dynamics*, edited by L. Angermann (IntechOpen, 2010).

[55] G. P. Baeza *et al.*, "Effect of grafting on rheology and structure of a simplified industrial nanocomposite silica/SBR," Macromolecules **46**(16), 6621–6633 (2013).

[56] T. Hashimoto and T. Kume, "'Butterfly' light scattering pattern in shear-enhanced concentration fluctuations in polymer solutions and anomaly at high shear rates," J. Phys. Soc. Jpn. **61**(6), 1839–1843 (1992).

[57] A. Fernández-Nieves, A. Fernández-Barbero, and F. de las Nieves, "Static light scattering from fractal aggregates of microgel particles," in *Trends Colloid Interface Science XVI* (Springer, 2004), pp. 251–254.

[58] J. Ramsay and P. Lindner, "Small-angle neutron scattering investigations of the structure of thixotropic dispersions of smectite clay colloids," Faraday Trans. **89**(23), 4207–4214 (1993).

[59] L. Campana, M. Bossy, and J. Bec, "Stochastic model for the alignment and tumbling of rigid fibres in two-dimensional turbulent shear flow," arXiv:2207.02649 (2022).

[60] Y.-G. Tao, W. K. den Otter, and W. J. Briels, "Kayaking and wagging of rods in shear flow," Phys. Rev. Lett. **95**(23), 237802 (2005).

[61] D. Xie *et al.*, "Shear induced alignment of low aspect ratio gold nanorods in Newtonian fluids," J. Phys. Chem. Lett. **6**(19), 3815–3820 (2015).

[62] J. Park and J. E. Butler, "Inhomogeneous distribution of a rigid fibre undergoing rectilinear flow between parallel walls at high Péclet numbers," J. Fluid Mech. **630**, 267 (2009).

[63] J. Ramsay, "Recent developments in the characterization of oxide sols using small angle neutron scattering techniques," Chem. Soc. Rev. **15**(3), 335–371 (1986).

[64] J. Goodwin and R. H. Ottewill, "Properties of concentrated colloidal dispersions," J. Chem. Soc., Faraday Trans. **87**, 357 (1991).

[65] L. Hilliou, D. Vlassopoulos, and M. Rehahn, "Dynamics of nondilute hairy-rod polymer solutions in simple shear flow," Macromolecules **34**(6), 1742–1750 (2001).

[66] S. K. Siddiquee and J. W. van Egmond, "The shear response of low molecular weight poly (n-hexyl isocyanate) wormlike three-arm stars in semidilute solution," Macromolecules **31**(8), 2661–2669 (1998).

[67] J. Lee *et al.*, "Investigation of shear-banding structure in wormlike micellar solution by point-wise flow-induced birefringence measurements," J. Rheol. **49**(2), 537–550 (2005).

[68] R. G. Egres, F. Nettesheim, and N. J. Wagner, "Rheo-SANS investigation of acicular-precipitated calcium carbonate colloidal suspensions through the shear thickening transition," J. Rheol. **50**(5), 685–709 (2006).

[69] C. Z. Liang, T.-S. Chung, and J.-Y. Lai, "A review of polymeric composite membranes for gas separation and energy production," Prog. Polym. Sci. **97**, 101141 (2019).

[70] H. R. Lim *et al.*, "Advanced soft materials, sensor integrations, and applications of wearable flexible hybrid electronics in healthcare, energy, and environment," Adv. Mater. **32**(15), 1901924 (2020).

[71] A. Koh *et al.*, "A soft, wearable microfluidic device for the capture, storage, and colorimetric sensing of sweat," Sci. Transl. Med. **8**(366), 366ra165 (2016).

[72] B. Xu *et al.*, "Nanocomposite hydrogels with high strength cross-linked by titania," RSC Adv. **3**(20), 7233–7236 (2013).

[73] D. Morales *et al.*, "Bending of responsive hydrogel sheets guided by field-assembled microparticle endoskeleton structures," Small **12**(17), 2283–2290 (2016).

[74] M. Mehrali *et al.*, "Nanoreinforced hydrogels for tissue engineering: Biomaterials that are compatible with load-bearing and electroactive tissues," Adv. Mater. **29**(8), 1603612 (2017).

[75] E. Prince *et al.*, "Biomimetic hydrogel supports initiation and growth of patient-derived breast tumor organoids," Nat. Commun. **13**(1), 1466 (2022).